A Multitemporal Method for Correction of Tropospheric Effects in Differential SAR Interferometry: Application to the Gulf of Corinth Earthquake

Ferdaous Chaabane, Antonio Avallone, Florence Tupin, Pierre Briole, and Henri Maître

***Abstract*—Tropospheric inhomogeneities can form a major error source in differential synthetic aperture radar interferometry measurements, which are used in slow-deformation monitoring. Indeed, variations of atmospheric conditions between two radar acquisitions produce variations in the signal path of two images and, thus, additional fringes on differential interferograms. These effects have a strong influence on interferograms and must be compensated to obtain reliable deformation measurements. This paper presents a methodological approach to reduce at both global and local scales tropospheric contributions directly from differential interferograms. It first requires refined knowledge of the stable scatterers that can only be obtained from the analysis of a large population of multitemporal interferograms. The correction of global-scale atmospheric contribution exploits the correlation between phase and topography. The correction of local artifacts is based on the correlation between interferograms containing one common acquisition. This technique is validated on a database of 81 differential interferograms covering the Gulf of Corinth (Greece) and used to improve the measurements of ground deformation compared to global positioning system measurements.**

***Index Terms*—Differential synthetic aperture radar interferometry (DinSAR), ground deformation, tropospheric effects.**

I. Introduction

SYNTHETIC aperture radar (SAR) and differential SAR interferometry (DinSAR) have proven to be performing tools for measuring topography profile and ground-surface motion with great accuracy (of the order of the wavelength).

The differential interferometric phase is obtained by combining three radar images and contains information only related to topographic changes. Since 1992, differential interferometry has improved considerably deformation measurements associated with earthquakes [1], ground movements [2], [3], volcanic eruptions [4], etc. However, the accuracy of this technique is compromised by atmospheric effects. Indeed, the microwave radar pulse undergoes an additional time delay when passing through the troposphere due to the index of refraction. Ionospheric effects (Faraday rotation) are not considered here because the wavelength is low enough (C-band). This phenomenon causes phase distortion in radar images. Thus, differential interferograms contain ground-deformation fringes mixed with tropospheric fringes. In order to avoid atmospheric effects from being misinterpreted as ground displacements, it is mandatory to evaluate their contribution and retrieve it from differential interferograms. In this paper, we will particularly study the impact of atmospheric disturbances to the interferometric measure. Previous studies have proposed methods to bypass the problem of atmospheric artifacts. Massonnet and Feigl [5] were the first to attribute unknown features in the interferograms of Mount Etna and Landers (CA, USA) to atmospheric variations. Since the publication of this paper, there has been a significant number of methods dedicated to atmospheric correction. They can be classified in three categories.

The first family of techniques is based on the knowledge of *auxiliary* data, such as pressure, temperature, water vapor, refractive index of the troposphere or ionosphere, etc., to estimate the atmospheric artifacts. Zebker *et al.* [6] propose a model of atmospheric effects and estimate the interferogram degradation observed in wet regions. Tarayre and Masonnet [7] propose a method that considers, in addition to tropospheric effects, the ionospheric effects, which are generally neglected.

Contrary to the first family, the second family of methods considers the atmospheric disturbances starting from the *interferometric phase* and the *geometrical data*. In many cases, we do not have meteorological information corresponding exactly to the date of acquisition or to the covered region. These methods suggest modeling and correcting the atmospheric contribution by using a database of several interferograms in order to increase the estimated precision. The approach suggested by Ferreti *et al.* [8] represents a complete method for the identification and exploitation of stable natural reflectors called

Manuscript received May 7, 2006; revised October 19, 2006. This paper was done during the Ph.D. years of F. Chaabane in the Signal and Image Department (TSI), Ecole Nationale Supérieure des Télécommunications (ENST), Paris, France, and during the Ph.D. years of A. Avallone in the Institut de Physique du Globe de Paris.

F. Chaabane is with the Mathématiques Appliquées, Signaux et Communications Department, Sup'Com, El Ghazala Ariana 2083, Tunis, and also with the Research Unit in Satellite Images and its Applications (URISA), Sup'Com, El Ghazala Ariana 2083, Tunis.

A. Avallone is with the Istituto Nazionale di Geofisica e Vulcanologia, 83035 Grottaminarda, Italy.

F. Tupin and H. Maître are with the TSI Department, ENST, 75634 Paris, France, and also with the Laboratoire Traitement et Communication de l'Information (LTCI), Unité Mixte de Recherche CNRS-GET/Télécom Paris (UMR 5141), 75634 Paris, France.

P. Briole is with the French National Center for Research (CNRS), 75794 Paris, France, and also with the Institut de Physique du Globe, 75252 Paris, France.

Color versions of one or more of the figures in this paper are available online at http://ieeexplore.ieee.org.

Digital Object Identifier 10.1109/TGRS.2007.894026

permanent scatterers (PS) starting from a time series of differential interferograms. This method provides good results in urban regions since the nature of the ground is closely related to the density of the PS.

The technique in [9] uses a different approach based on the phase gradient average but still starts from a time series of several interferograms. The performances of this method remain dependent on the number of considered interferograms.

The third family of approaches estimates the atmospheric phase delay directly starting from several interferograms covering the same region. These methods have the advantage of being independent of auxiliary data, but they process under some assumptions related to physical properties. These assumptions will make it possible to choose a model for atmospheric disturbances. The study of the atmospheric effects is then carried out, starting from the intrinsic image analysis.

Beauducel *et al.* [10] propose a method of differential atmospheric correction starting from a correlation between the interferometric phase and the altitude. This technique consists in applying a simultaneous inversion of a deformation and a tropospheric model (ionospheric effects are neglected) for a database of several interferograms. This method preserves the advantages of a simple and direct method. However, the obtained accuracy remains weak compared to previous methods. This is primarily due to the fact that the deformation model is of the first order and that the method of tropospheric correction needs to be more rigorous. The technique in [11] has the advantage of being independent of any deformation or tropospheric model. In case of a time series of several interferograms covering the same region, a method to estimate atmospheric effects is to use the correlations between interferograms derived from two SAR couples that have one master common image. However, the performances are directly related to interferogram quality.

The work proposed in this paper presents a fusion of improved versions of the two techniques presented previously when a data set of multitemporal interferograms is available. The proposed method proceeds in two main steps: The first step is dedicated to the estimation of global tropospheric effects. This is done with two phases: First, a subset of very coherent pixels is identified using a correlation between the phase value and topography. These pixels allow the computation of a global tropospheric model for each interferogram. Second, a cross validation of the models is applied using the entire multitemporal database. Since multiple interferograms are available, a method can be developed for the validation of tropospheric models using a triplet of interferometric pairs containing one common acquisition. Indeed, it can be shown that an algebraic relationship between the parameters of the tropospheric models exists. The second step is dedicated to the estimation of local tropospheric effects. The methodology based on the correlation between interferograms that contain one common acquisition proposed in [11] is improved. The modeled tropospheric effects are then removed from each interferogram. This technique was tested on a database of 81 differential interferograms of the Gulf of Corinth and used to improve the measurement of ground deformation compared to global positioning system (GPS) measurements.

The structure of this paper is given as follows: The second and the third sections describe in detail the correction method, while the fourth section is dedicated to the result presentation

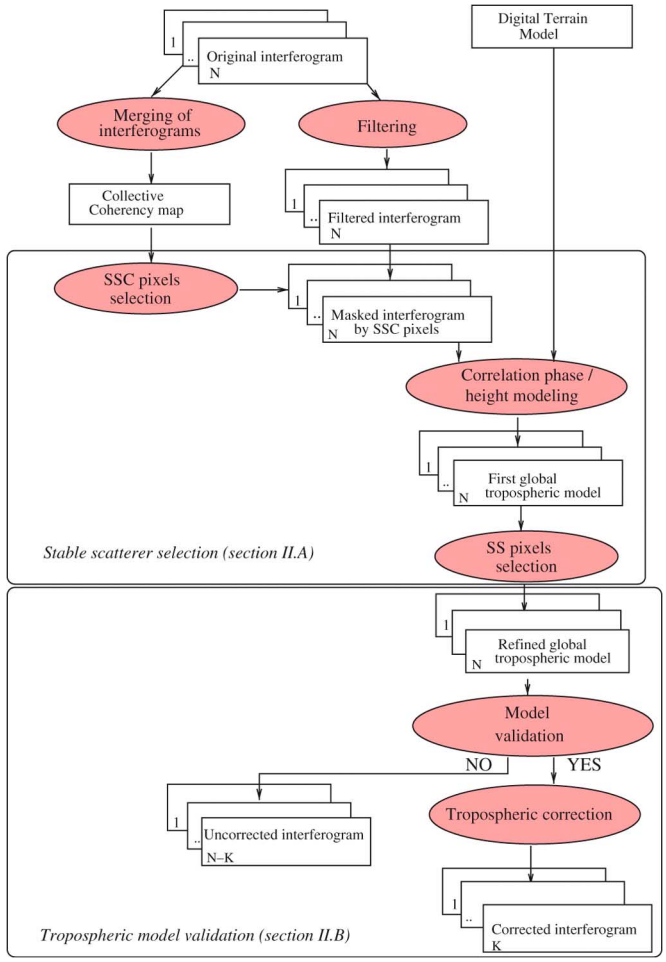

Fig. 1. Block diagram representing the main steps of estimation of global tropospheric effects.

on the Gulf of Corinth (Greece). The second section deals with global tropospheric disturbances. We present the two main steps that allow the computation of reliable models, namely 1) selection of stable scatterers (SSs) and 2) tropospheric model validation. The third section is dedicated to local atmospheric disturbances starting from interferograms corrected from the global effects. The last section summarizes some results obtained by applying this approach to a data set of multitemporal interferograms covering the Gulf of Corinth and highlights the improvement of ground-deformation precision after atmospheric effects correction. Finally, a section is dedicated to the interests and limits of the proposed method.

II. Estimation of the Global Tropospheric Effects

The block diagram describing the main steps of the estimation of global tropospheric effects is presented in Fig. 1.

A. Selection of SSs

This section presents the tropospheric model used and describes different steps for the identification of SSs. There are three main steps, which are detailed here. First, stable-pixel candidates are selected, and a preliminary tropospheric model is derived. Both stable pixels and tropospheric models are then

refined by selecting a more reliable subset of pixels. Second, the refined tropospheric models are validated (or rejected) by cross validation. Third, the interferometric phase is corrected before the local correction step.

It can be shown that tropospheric effects are correlated with topography. Indeed, if the troposphere is assumed to be horizontally homogeneous, the variations of the phase signal are due to changes of temperature, pressure, and water vapor, which are only related to the thickness of the atmosphere, i.e., to altitude. In this paper, we propose to estimate and correct these tropospheric effects by modeling the correlation between the wrapped phase and altitude using a linear model [10].

However, the analysis of the phase/altitude regression requires the selection of a subset of pixels that maintain their coherence [12] over long time intervals in order to better discern the different signals that concur to the interferometric phase.

This selection is done in two steps: First, using the local phase stability, a subset of candidates is detected; then, a second selection is done using only the pixels that fit the proposed tropospheric model.

Let us note here that the pixels we are looking for are characterized by their local phase stability in many interferograms. Thus, they do not correspond to the PSs as first defined in [8] using a punctual amplitude criterion. These pixels are herein called "stable scatterers."

1) Preselection of Stable Pixels: First, a collective "coherency"[1] map is produced, starting from all available differential interferograms in order to identify the first subset of stable pixels [stable scatterer candidates, (SSCs)]. Instead of using directly the coherence images of the interferograms, the phase gradient method proposed in [10] has been used for each interferogram. This technique consists in computing within a 3×3 pixel square the difference of phase values between each pixel and the eight contiguous ones. For each pixel, the phase difference with the eight neighbors is compared to a threshold value, and the coherency is given by the number of neighbors that differ from the central value by less than the threshold. Several tests have been carried out with different gradient thresholds. Low values of the gradient threshold produced a collective coherence map that is too permissive with a very large population of SSCs, even in classical low-coherency areas (vegetated area, cultivated fields, etc.); on the other hand, high values of gradient threshold produced a collective coherence map that is too strict with a not statistically significant number of SSC. We fixed the gradient threshold to 16% of the 2π phase over 25-m pixel (0.04 rad/m) because it represented a good tradeoff between a statistically opportune population of SSCs and the surface geology response to the SAR wavelength.

Then, the pixels are classified depending on their local stability, and all the results for the whole database are combined into one image using a mean operation (Fig. 2). This image, which is herein called the coherency map, is eventually thresholded to provide a binary map of the SSC pixels.

The interest of this global mask is that it merges a large number of images, and consequently, it is expected to be less affected by local and temporal effects related to deformations or local tropospheric effects. In addition, the obtained image reduces the number of pixels used for the calculation of the tropospheric models from a few millions to a few thousands.

2) Estimation of the Tropospheric Model: The interferograms are first filtered to reduce the wrapped phase noise. The filtering process applies a local compensation of the terrain slope based on a multispectral estimation of the 2-D sinusoid described by two frequencies of the complex phase signal [13]. By reducing the noise in the interferograms, the filtered phase allows a more reliable modeling of the phase/altitude correlation. The improvement of the modeling of the tropospheric effects using this filtering technique was proven in previous work [14]. Indeed, filtering decreases the mean square error (MSE) between the observations and the estimated model. Let us note that this filtering method assumes local stationarity of the phase signal, which is the case for the SSC pixels previously defined (local phase stability).

Fig. 3 shows the temporal distribution of coherence (according to the interferogram time period) plotted for SSC pixels and for non-SSC pixels. On the one hand, we can notice that the SSC-pixel coherence random variable is more stable. On the other hand, we can see the coherence exponential decrease according to interferogram time period for the two curves.

Applying the obtained mask on each interferogram, we study the relationship between the wrapped filtered phase of the SSC pixels and the elevation extracted from the digital elevation model (which can be derived either by optical or interferometric measures). A simple analysis [15] indicates that a correlation between topography and phase exists and can be estimated with a linear model $(\alpha_{\text{opt}}, \beta_{\text{opt}})$. The phase related to global atmospheric effects is modeled by

$$\Phi_{\text{glob}} = \alpha_{\text{opt}} h + \beta_{\text{opt}}. \tag{1}$$

First, α_{opt} is estimated. The optimization proceeds in the complex domain to avoid additional errors due to phase unwrapping [14], i.e.,

$$\alpha_{\text{opt}} = \arg \max_{\alpha \in [-1,1]} L_1(\alpha) \tag{2}$$

$$L_1(\alpha) = \frac{\left| \sum_i w_i e^{-j2\pi(\phi^i_{\text{obs}} - \alpha h^i)} \right|}{\left| \sum_i w_i \right|}. \tag{3}$$

The coherency mask values are used as weight w_i for each pixel SSC. This expression is maximized when all the vectors are aligned, implying that $\phi^i_{\text{obs}} - \alpha h^i$ is constant.

The search is done in an exhaustive way for values of α_{opt} in $[-1, 1]$ with a step of 0.01. Second, the value of β_{opt} is estimated while varying α on a small interval around α_{opt} and by minimizing the weighted MSE, i.e.,

$$\beta_{\text{opt}} = \min_{\beta \in [-2\pi, 2\pi], \alpha \in [\alpha_{\text{opt}} \pm \epsilon]} L_2(\beta) \tag{4}$$

$$L_2(\beta) = \frac{1}{N} \sum_i w_i \left(\phi^i_{\text{obs}} - \left[(\alpha h^i + \beta) - E\left((\alpha h^i + \beta)/2\pi \right) * 2\pi \right] \right)^2 \tag{5}$$

where $E(x)$ is the closest integer value of x.

The estimation of the two parameters is done separately to minimize the computing time. This first estimation of the linear model parameters is not sufficient. Indeed, in spite of their great

[1]The map is called a collective "coherency" map in the following, although the coherence is not directly used to compute it.

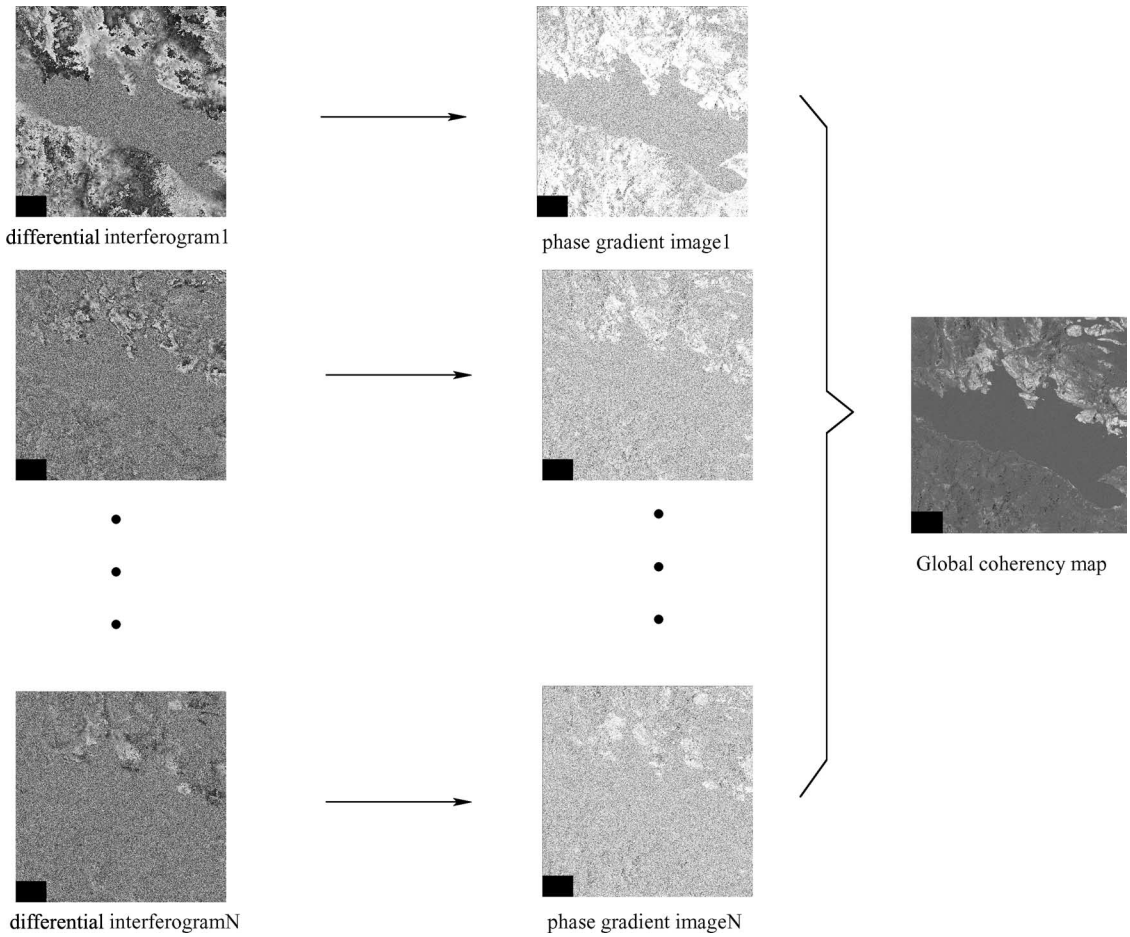

Fig. 2. Global "coherency" map computation. The individual phase stability images obtained directly from interferograms are stacked and scaled to the 0–255 range.

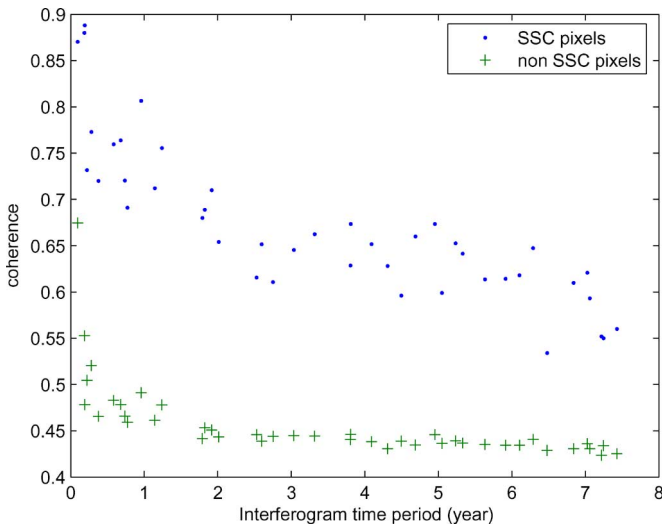

Fig. 3. Temporal distribution of coherence plotted for SSC pixels and non-SSC pixels. The number of non-SSC pixels is more significant than the SSC pixels, which explains why their temporal distribution is smoother.

coherence, SSC pixels are not robust enough compared to the calculated model of the troposphere. This is especially due to local atmospheric disturbances.

3) Refined Selection of Stable Scatterers Using the Tropospheric Model: Among the pixel candidates, the scatterers that are in accordance with the proposed model the most are selected to define the SS set.

First, the best fitting models (with low MSE) are selected. This defines a subset of K interferograms characterized by a strong correlation between the phase and altitude, which is denoted by S_{SS}. For each selected interferogram k and for each SSC pixel i, the error ϵ_i^k between filtered phase ϕ_i^k and modeled phase $(\hat{\phi}_k^{\mathrm{glob}})^i$ is computed, i.e.,

$$\epsilon_i^k = \phi_i^k - \left(\hat{\phi}_k^{\mathrm{glob}}\right)^i \quad [2\pi]. \tag{6}$$

All the ϵ_i^ks for the K interferograms of S_{SS} are merged using the symmetrical sum [16] σ_0 to obtain the global error ϵ_i, i.e.,

$$\epsilon_i = \sigma_0\left(\sigma_0\left(\ldots,\sigma_0\left(\sigma_0\left(\epsilon_i^1,\epsilon_i^2\right),\epsilon_i^3\right)\ldots,\epsilon_i^k\right)\ldots\right),\epsilon_i^K\right). \tag{7}$$

The fusion operator σ_0 has the advantage of being very selective. The lowest values of ϵ_i^k for as many models as possible identify the most coherent pixels and, therefore, the SSs of the region. This method expresses the multitemporal robustness of the SS pixels that are used to perform a more reliable global tropospheric model estimation. For all the differential interferograms, α_{opt} and β_{opt} are thus reestimated by a new optimization of L_1 and L_2 functions [(3) and (5)]. The improvements are evaluated in terms of MSE decrease.

B. Tropospheric Model Validation

The second step of the global atmospheric effect estimation is the validation of the obtained tropospheric models. Let us consider the following formulation of the differential interferometric phase:

$$\begin{aligned}\Phi &= \Phi_{\text{glob}} + \Phi_{\text{loc}} + \Phi_{\text{gr}} + \Phi_{\text{no}} \\ &= (\alpha_{\text{opt}} h + \beta_{\text{opt}}) + \Phi_{\text{loc}} + \Phi_{\text{gr}} + \Phi_{\text{no}} \end{aligned} \tag{8}$$

where Φ_{glob} represents the global tropospheric contribution modeled by $\alpha_{\text{opt}} h + \beta_{\text{opt}}$ according to the previous analysis, Φ_{loc} is the contribution of the local tropospheric artifacts, Φ_{gr} is related to ground displacements, and noise term Φ_{no} includes errors related to both topographic and orbital corrections, and temporal and space decorrelation not corrected by filtering.

The first term Φ_{glob} is assumed to be independent of the three other terms, i.e., local disturbances, ground movement, and interferometric noise are not correlated with altitude h. For each triplet of interferograms ϕ_{AB}, ϕ_{BC}, and ϕ_{AC} obtained starting from three images A, B, and C, a vectorial relationship exists between the parameters of the tropospheric model, i.e.,

$$\phi_{\text{AC}} = \phi_{\text{AB}} + \phi_{\text{BC}} => \alpha_{\text{opt}_{\text{AB}}} + \alpha_{\text{opt}_{\text{BC}}} = \alpha_{\text{opt}_{\text{AC}}}. \tag{9}$$

This relationship is similar to the second Kirchoff law. In our case, we use here a usual vocabulary of the graph theory where each arc corresponds to an interferogram and each circuit (or graph) identifies a subset of interferograms connected with a common SAR image. Thus, the algebraic sum of the parameters α_{opt} along a circuit is constantly equal to zero. If it is not the case, that means that the parameters have been badly estimated and should be corrected.

The vectorial relation given by (9) highlights the multitemporal aspect of our approach. The application of this relationship is performed using the algorithm of Bellman–Ford [17], which solves the shortest path problem. This algorithm progressively decreases the weight of the current path from the source to each vertex until it achieves the shortest path. In addition, it returns "True" if the given graph contains no negative cycles that are reachable from the source; otherwise, it returns "False." Thus, this algorithm can verify if the sum of the parameters is zero in all the circuits.

The initial graph is made up of arcs corresponding to the parameters of the tropospheric models selected for the identification of SS pixels, i.e., the graph related to S_{SS} interferograms. These parameters are assumed to be valid since they have a low MSE and will be used to validate the other models. Validation algorithm consists on checking that the sum of the parameters in all possible circuits is zero every time we add an arc to the initial graph. This is carried out by applying twice the Bellman–Ford algorithm.

Indeed, applying this algorithm on the current graph, circuits of negative cost can be detected, and by reversing the sign of each parameter on the arcs, circuits of positive cost can also be detected. Briefly, if the Bellman–Ford algorithm detects no circuit of negative cost, then (neither for the original graph nor for that where the sign of each value is reversed) it means that all the circuits are of zero cost.

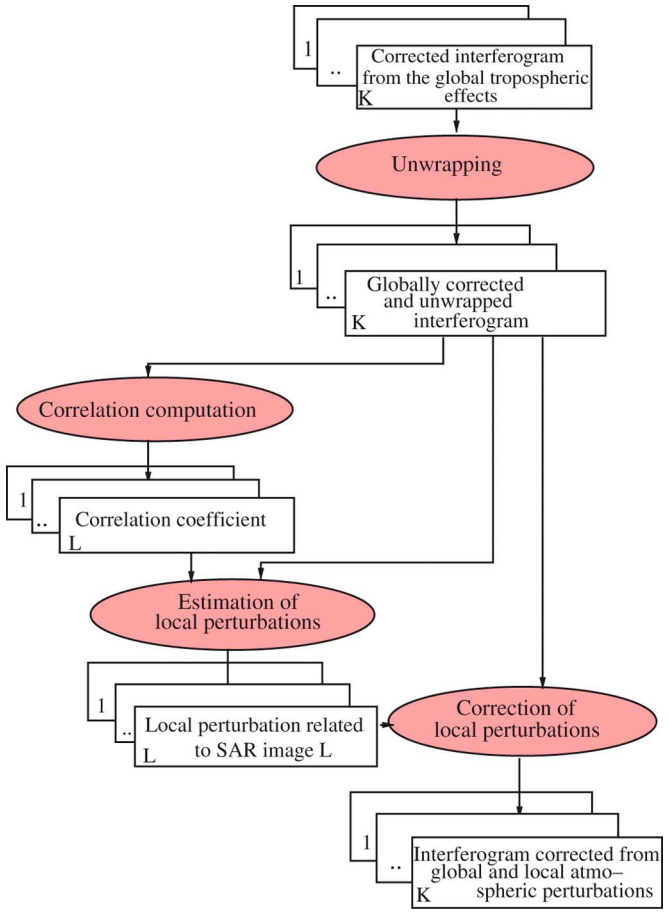

Fig. 4. Block diagram representing the main steps of estimation of local atmospheric effects.

The Bellman–Ford algorithm allows us to validate the previously obtained global tropospheric models and to reject nonreliable estimations. In addition, it underlines the interest of SS pixel selection on SSC pixels by increasing the number of validated models.

Finally, differential interferograms are corrected from global atmospheric effect by subtracting the tropospheric model phase Φ_{glob} from the wrapped filtered phase, i.e.,

$$\Phi_1 = \Phi - \Phi_{\text{glob}} = \Phi_{\text{loc}} + \Phi_{\text{gr}} + \Phi_{\text{no}}. \tag{10}$$

III. Estimation of Local Tropospheric Effects

At this step of processing, we have a database of several interferograms filtered and corrected from global tropospheric effects. However, the assumption of the horizontal homogeneity of troposphere is not always valid because the weather conditions (clouds, storms, winds, etc.) will not be the same in two nonsimultaneous acquisitions. This phenomenon causes local disturbances in differential interferograms. To solve this problem, an approach first introduced by Sarti *et al.* [11] has been adapted and improved. It is based on the correlation between differential interferograms having a common SAR acquisition. The block diagram describing the various steps of the local atmospheric effect estimation is shown Fig. 4.

The local tropospheric contributions are estimated in three main phases. First, the interferograms are unwrapped to remove the phase ambiguity. Then, a local complex correlation is computed between the interferograms containing one common acquisition [11] in order to retrieve the local phase anomalies related to each SAR image.

A. Phase Unwrapping

Local atmospheric effects cannot be estimated starting only from one interferogram. Thus, the phase ambiguity represents a major problem in the use of several interferograms to estimate these perturbations. For this reason, the interferograms are unwrapped using a weighted least squares algorithm [18]. It is a global unwrapping technique that computes the exact value of the interferometric phase starting from the phase differences or the local frequencies [19]. The addition of weights reflects confidence in the measurement of the phase differences (or the local frequencies) in each pixel of the image. A binary weight computed from the collective coherence mask by thresholding is used in this paper because of the significant number of interferograms. The threshold is empirically chosen as a compromise between the quality (coherence) and size of the selected regions.

B. Complex Correlation Between Interferograms

Correlation is computed by selecting triplets of interferograms covering a period before or after the deformation event. The processing is applied to the interferograms that do not contain seismic deformation because it can bend the estimation of local effects. However, this aspect does not represent a limit because the phase anomalies related to each SAR image will be subtracted from all the interferograms of our database.

Considering a triplet of unwrapped interferograms AB, AC, and BC, a complex correlation weighted by the coherence between the complex signals is computed. For each image, the correlation coefficient is calculated in the following way (for example, for SAR, image A):

$$\rho_A = \frac{E(xy^*) - E(x)E(y^*)}{\sigma_x \sigma_y} \tag{11}$$

where $x = M_{\mathrm{AB}} e^{j\phi_{\mathrm{AB}}}$, $y = M_{\mathrm{AC}} e^{j\phi_{\mathrm{AC}}}$, M_{AX} represents the coherence value, ϕ_{AX} corresponds to the interferograms containing image A, and $\sigma_x^2 = E|x|^2 - |E(x)|^2$.

The size of the moving window for computing the statistics depends on the size of the local disturbances, which are generally visible on interferograms derived from a common SAR image. Once the coefficients of correlation for each triplet of interferograms are calculated, we estimate the local atmospheric disturbances related to each SAR image. Contrary to the approach suggested in [11], the effects related to one SAR image A are considered, starting from its correlation ratio and from all the unwrapped interferograms AX that contain A and not only from one of them.

C. Local Artifacts Estimation

At this step, the correlation coefficients ρ_A, ρ_B, and ρ_C are calculated for a triplet of interferograms AB, BC, and AC. The contribution of the local phase anomalies related to image A are normally present only in interferograms AB and AC. It should result in a high value (close to 1) of ρ_A and, conversely, in low values (close to 0) of ρ_B and ρ_C. This condition is analytically represented using a sigmoid function, i.e.,

$$C_A^{\mathrm{AB}} = s(\rho_A) s(1 - \rho_B)(unw_{\mathrm{AB}} - [unw_{\mathrm{AB}}])_W \tag{12}$$

where s is the sigmoid function and unw_{AB} and $[unw_{\mathrm{AB}}]$ correspond to the unwrapped phase AB and the averaged phase value in window W, respectively. Removing the averaged phase value allows us to estimate only the high-frequency contributions.

However, a single triplet could not put in evidence all the local phase anomalies of a given image A. Therefore, all the contributions $C_A^{\mathrm{AX}_i}$ obtained from N interferograms AX_i containing that image are combined using a maximum operator, i.e.,

$$C_A = \max_{i=1}^{\mathrm{Card(S)}} C_A^{\mathrm{AX}_i}. \tag{13}$$

Thus, all the information of interferograms AX_i are used to compute the local contributions related to image A. Furthermore, we notice that the previous correction of a homogeneous tropospheric effect (at global scale) enhances high-frequency local tropospheric heterogeneities, which are now easier to extract.

Finally, the interferograms corrected of the global atmospheric effects are corrected from local effects according to

$$\Phi_2 = \Phi_1 - \Phi_{\mathrm{loc}} = \Phi_1 - \left(C_M^{\mathrm{loc}} - C_S^{\mathrm{loc}}\right) = \Phi_{\mathrm{gr}} + \Phi_{\mathrm{no}} \tag{14}$$

where C_M and C_S are the local contributions relating to the master and slave images, respectively.

IV. Application to Gulf of Corinth Earthquake

The methodology presented previously has been tested on 81 European Remote Sensing 1 and 2 (ERS-1/2) differential interferograms of the Gulf of Corinth computed from 38 ERS satellite images acquired on three different tracks (Table I). The interferograms cover variable time spans (1 day to 7.42 years) in the period of 1992–1999. Both the 1992 Ms $= 5.9$ Galaxidi earthquake and the 1995 Ms $= 6.2$ Aigion event are covered by the data (see Figs. 5 and 6).

A. Estimation of the Global Tropospheric Effects

The first step is the selection of SS pixels. Fig. 7 shows the coherency map corresponding to the east track of Gulf of Corinth calculated from a set of 43 interferograms. As we can see, the obtained image gives prominence to SSC pixels (black ones) and reduces the number of pixels used for the calculation of tropospheric models. Applying the global mask on the filtered interferograms, we estimate the tropospheric model using the correlation between the wrapped phase and the elevation.

Fig. 8 shows an example of two phase/altitude correlation for two interferograms selected from the subset S_{SS}. First, the troposphere is modeled using SSC pixels [Fig. 8(a) and (c)] and then using SS pixels [Fig. 8(b) and (d)]. The phase values of

TABLE I
GULF OF CORINTH ERS IMAGE FEATURES. THE ACQUISITION DATES ARE FROM JUNE 1992 TO AUGUST 2000, ON TWO DIFFERENT ORBITS AND THREE DIFFERENT TRACKS (FIG. 6)

Satellite	N.orbite	Date	Time	Sense	Track	Frame
ERS1	4661	06/06/92	9h13 TU	D	7	2835
ERS1	5162	11/07/92	9h13 TU	D	7	2835
ERS1	5663	15/08/92	9h13 TU	D	7	2835
ERS1	6164	19/09/92	9h13 TU	D	7	2835
ERS1	6665	24/10/92	9h13 TU	D	7	2835
ERS1	10172	26/06/93	9h13 TU	D	7	2835
ERS1	19534	10/04/	9h13 TU	D	7	2835
ERS1	22039	02/10/95	9h13 TU	D	7	2835
ERS1	43081	11/10/99	9h13 TU	D	7	2835
ERS2	5873	04/06/96	9h13 TU	D	7	2835
ERS2	6374	09/07/96	9h13 TU	D	7	2835
ERS2	12386	02/09/97	9h13 TU	D	7	2835
ERS2	12887	07/10/97	9h13 TU	D	7	2835
ERS2	15893	05/05/	9h13 TU	D	7	2835
ERS2	22406	03/08/99	9h13 TU	D	7	2835
ERS2	24410	21/12/	9h13 TU	D	7	2835
ERS1	6937	12/11/92	9h15 TU	D	279	2835
ERS1	9943	10/06/93	9h15 TU	D	279	2835
ERS1	10945	19/08/93	9h15 TU	D	279	2835
ERS1	19806	29/04/95	9h15 TU	D	279	2835
ERS1	20808	08/07/95	9h15 TU	D	279	2835
ERS2	1135	09/07/95	9h15 TU	D	279	2835
ERS2	1636	13/08/95	9h15 TU	D	279	2835
ERS2	2137	17/09/95	9h15 TU	D	279	2835
ERS2	5644	19/05/96	9h15 TU	D	279	2835
ERS2	7147	01/09/	9h15 TU	D	279	2835
ERS2	7648	06/10/96	9h15 TU	D	279	2835
ERS2	8650	15/12/96	9h15 TU	D	279	2835
ERS2	10654	04/05/97	9h15 TU	D	279	2835
ERS2	12157	17/08/97	9h15 TU	D	279	2835
ERS2	21676	13/08/99	9h15 TU	D	279	2835
ERS1	9578	15/05/93	20h48 TU	A	415	765
ERS1	10079	19/07/93	20h48 TU	A	415	765
ERS2	770	13/06/95	20h48 TU	A	415	765
ERS2	1271	18/07/95	20h48 TU	A	415	765
ERS2	20810	13/04/99	20h48 TU	A	415	765
ERS2	26822	06/06/00	20h48 TU	A	415	765
ERS2	27824	15/08/00	20h48 TU	A	415	765

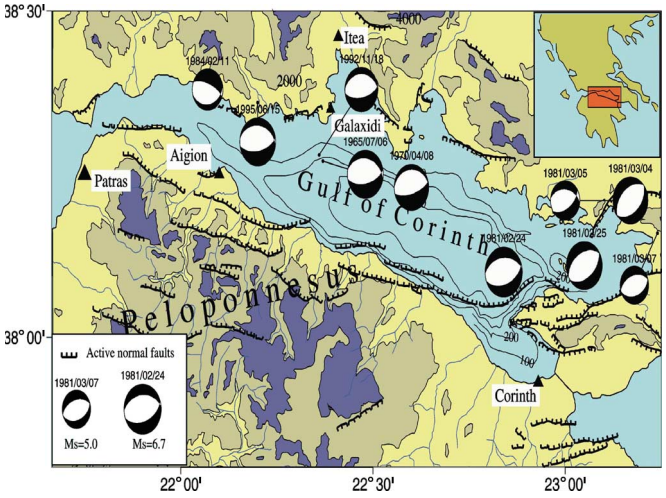

Fig. 5. Seismic map of Gulf of Corinth presenting main active rifts and all strong earthquakes that have occurred in this region since 1981.

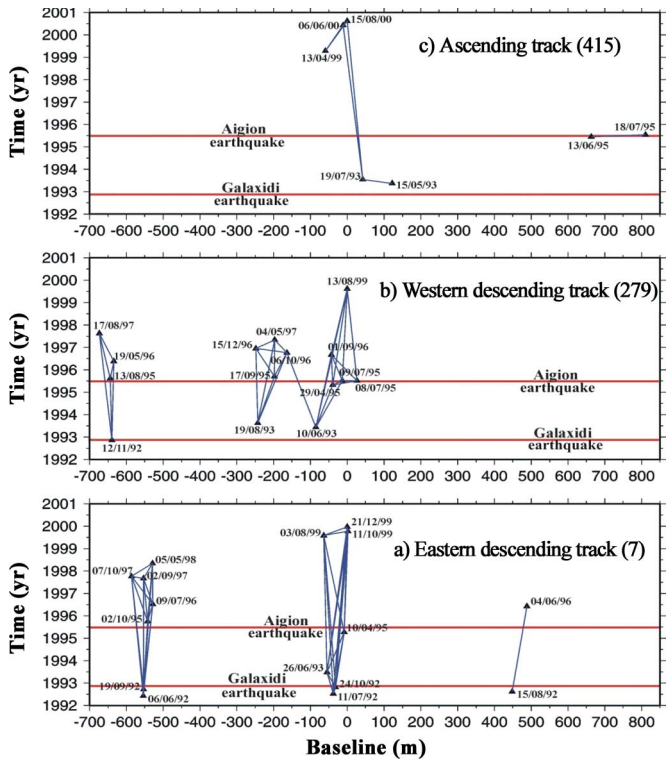

Fig. 6. ERS image and interferogram data set temporal distribution. Because of the baseline limitation ($<$ 100 m), only 81 interferograms (7 for track a, 31 for track b, and 43 for track c) are considered (blue lines). Both the 1992 Ms $=$ 5.9 Galaxidi earthquake and the 1995 Ms $=$ 6.2 Aigion event are covered (red lines).

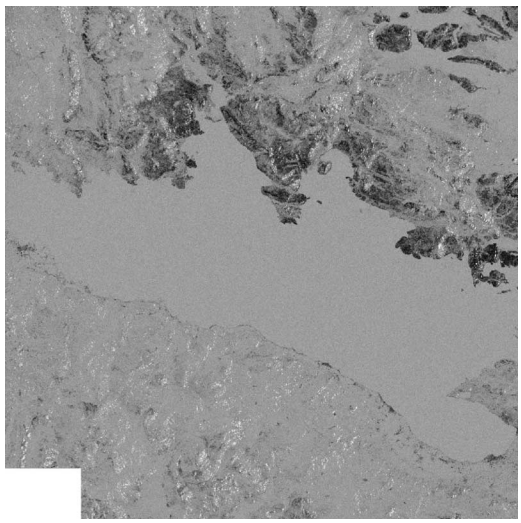

Fig. 7. "Coherency" map corresponding to the east track of Gulf of Corinth calculated from a set of 43 interferograms (in reverse video).

the SS pixels allow us to determine a linear model that better fits the phase/elevation regression. The improvement of the SS pixel selection is measured by means of the MSE. We notice the considerable decrease of the MSE and the readjustment of the parameters of the tropospheric model. These results are expected since the models of the S_{SS} interferograms are used for the selection of SS pixels.

Moreover, Fig. 9 illustrates the phase/altitude correlation for two interferograms not belonging to subset S_{SS}, first using the

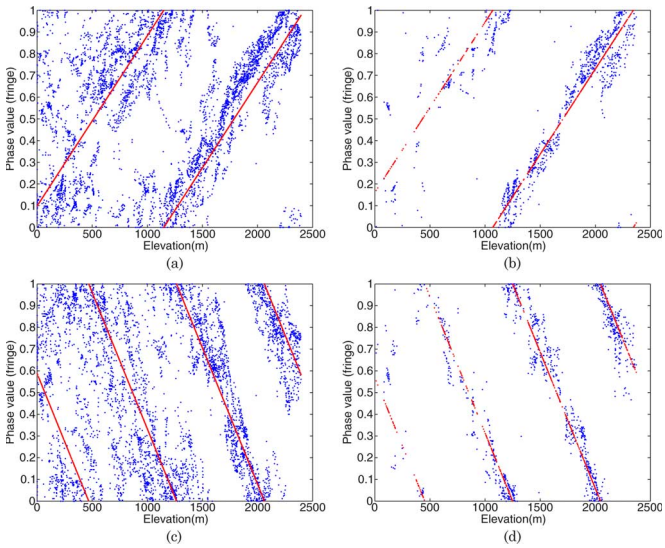

Fig. 8. SS pixel exploitation. Case of two interferograms belonging to the S_{SS} subset. (a) and (c) Phase/elevation regression starting from SSC pixels. (b) and (d) Phase/elevation regression starting from SS pixels for the same interferograms. (a) EQM $= 0.0358$, $\hat{\alpha_{\mathrm{opt}}} = 0.2$, and $\hat{\beta_{\mathrm{opt}}} = 25$. (b) EQM $= 0.0117$, $\hat{\alpha_{\mathrm{opt}}} = 0.2$, and $\hat{\beta_{\mathrm{opt}}} = 41$. (c) EQM $= 0.0448$, $\hat{\alpha_{\mathrm{opt}}} = -0.32$, and $\hat{\beta_{\mathrm{opt}}} = 105$. (d) EQM $= 0.0094$, $\hat{\alpha_{\mathrm{opt}}} = -0.32$, and $\hat{\beta_{\mathrm{opt}}} = 110$.

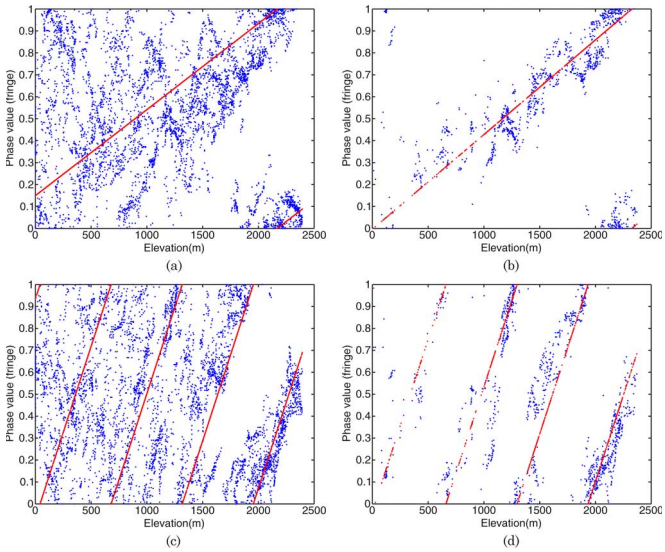

Fig. 9. SS pixel exploitation. Case of two interferograms not belonging to the S_{SS} subset and presenting average correlation. (a) and (c) Phase/elevation regression starting from SSC pixels. (b) and (d) Phase/elevation regression starting from SS pixels for the same interferograms. (a) EQM $= 0.0511$, $\hat{\alpha_{\mathrm{opt}}} = 0.1$, and $\hat{\beta_{\mathrm{opt}}} = 38$. (b) EQM $= 0.0094$, $\hat{\alpha_{\mathrm{opt}}} = 0.11$, and $\hat{\beta_{\mathrm{opt}}} = 254$. (c) EQM $= 0.0534$, $\hat{\alpha_{\mathrm{opt}}} = 0.41$, and $\hat{\beta_{\mathrm{opt}}} = 238$. (d) EQM $= 0.0210$, $\hat{\alpha_{\mathrm{opt}}} = 0.4$, and $\hat{\beta_{\mathrm{opt}}} = 246$. These two estimations are validated using the Bellman–Ford algorithm (see Section II-B).

SSC pixels [Fig. 9(a) and (c)] and then the SS pixels. As we can see, the filtering of the SSC pixels improves the model estimation with a clear decrease of the MSE.

In comparison with Figs. 8–10 shows an example of two interferograms not belonging to subset S_{SS} and presenting a poor correlation, which induced bad modeling. It is clear in this case that the use of SSC pixels is insufficient. According to this figure, we can notice that the identification of SS pixels shows a new orientation of the phase/altitude correlation. Using the

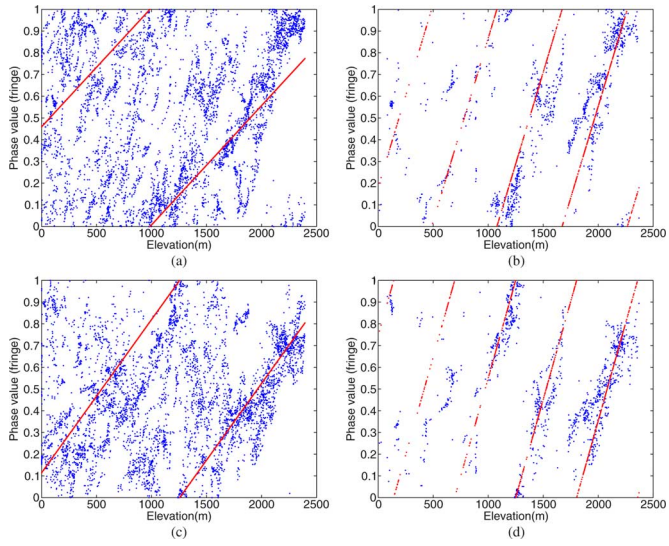

Fig. 10. SS pixel exploitation. Case of two interferograms not belonging to the S_{SS} subset and presenting poor correlation. (a) and (c) Phase/elevation regression starting from SSC pixels. (b) and (d) Phase/elevation regression starting from SS pixels for the same interferograms. (a) EQM $= 0.0632$, $\hat{\alpha_{\mathrm{opt}}} = 0.14$, and $\hat{\beta_{\mathrm{opt}}} = 117$. (b) EQM $= 0.0296$, $\hat{\alpha_{\mathrm{opt}}} = 0.43$, and $\hat{\beta_{\mathrm{opt}}} = 46$. (c) EQM $= 0.0619$, $\hat{\alpha_{\mathrm{opt}}} = 0.18$, and $\hat{\beta_{\mathrm{opt}}} = 29$. (d) EQM $= 0.0303$, $\hat{\alpha_{\mathrm{opt}}} = 0.44$, and $\hat{\beta_{\mathrm{opt}}} = 190$. These two estimations are validated using the Bellman–Ford algorithm (see Section II-B).

validation method, we can demonstrate that the new parameters of the model are optimal parameters.

The second step of the global tropospheric effect is the validation of the obtained models. Using the vectorial relation [see (9)] existing between the parameters of the tropospheric models, we can determine the correct models and reject the nonreliable estimations. Fig. 11 shows the progress of the validation algorithm applied on a subset of 21 interferograms covering the Gulf of Corinth. The Bellman–Ford algorithm verifies if all the circuits are of zero cost; if they are not, it detects the badly estimated parameters.

The validation algorithm reduces the number of interferograms to be exploited for the measurement of the deformation of ground from 81 to 43 interferograms. In order to correct the interferograms from tropospheric effects, the modeled phase is directly retrieved from the filtered and unwrapped phase.

B. *Estimation of Local Atmospheric Effects*

At this step of processing, among the 81 original interferograms, a set of 43 was validated and corrected from global tropospheric effects. Then, local atmospheric correction is applied to interferograms that do not contain seismic deformation because it can bend the estimation of local effects. However, this aspect does not represent a limit because the phase anomalies related to each SAR image will be subtracted from all the interferograms of our database. Fig. 12 shows an example of an unwrapped interferogram before and after the retrieval of local atmospheric contributions corresponding separately to the master and slave SAR images. Fig. 12(c) illustrates an atmospheric coastal effect, which have been detected and corrected by our methodology. We can also notice that the corrected interferogram is smoother than the noncorrected one. Furthermore, we notice that the previous correction of a

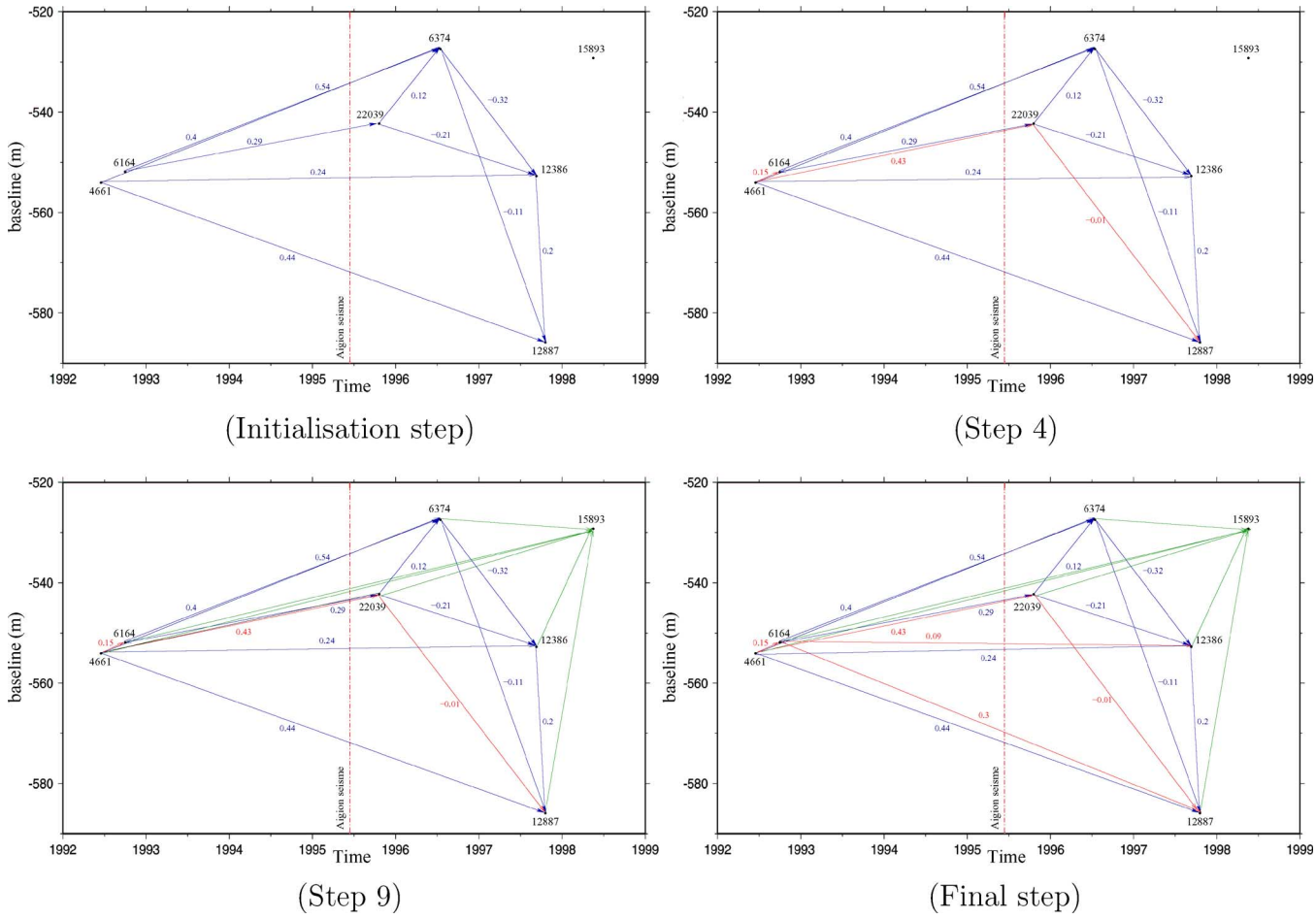

Fig. 11. Progress of the global tropospheric validation algorithm for a subset of 21 interferograms. Initialization step: The initial graph contains arcs corresponding to interferograms belonging to the S_{SS} subset (blue arcs). These arc values verify the vectorial relation [see (9)] and are useful for the validation of the other arcs. Step 4: We notice from this graph that three arcs are treated and validated (red arcs) since the cost is zero in all the circuits. Step 9: At this processing step, the algorithm has detected six arcs that cannot be validated (green arcs) since they do not belong to any circuits. Final step: The algorithm gives the final decision for all the arcs of the graph, i.e., the parameters of the global tropospheric effects for each interferogram. Results: 0 badly estimated arcs, 15 validated arcs, and 6 nonattributed arcs.

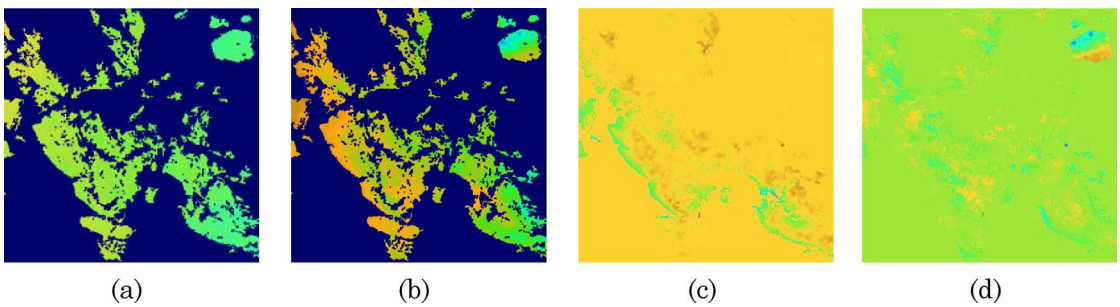

Fig. 12. Interferogram AB (a) before and (b) after local tropospheric correction. (c) and (d) Local tropospheric contributions determined for the SAR image A and the SAR image B, respectively.

homogeneous tropospheric effect (at global scale) enhances the high-frequency local tropospheric heterogeneities.

C. Evaluation of Local and Global Corrections

Once the harmful effects due to the atmosphere (global and local) are corrected, it remains to be no further than information relating to ground displacement and residual noise from the various corrections. In order to compensate the residual noise and increase confidence in the measurement of ground deformation, we carry out a simple average between the corrected interferograms since the seismic deformation is a specific event. The resulting stacked interferogram gives information about the amount of displacement for an average period.

In order to measure the deformation related to the earthquake in Aigion, Greece, it is necessary to fix the phase value corresponding to zero deformation. The stacking makes this task easier because of the error compensation. The zero-deformation value is then given, starting from the average phase values of the SS pixels, since they were used to

TABLE II
COMPARISON BETWEEN INSAR (WITHOUT AND WITH ATMOSPHERIC CORRECTION) AND GPS RESULTS

Point	GPS (mm)	InSAR(mm) without correction	InSAR(mm) with correction
B	7± 16	-30.8 ± 23.3	-26.3 ± 19.8
C	-202 ± 17	-179.8 ± 29.6	-204.4 ± 23.9
CT	-1 ± 13	-16.8 ± 15.2	10.0 ± 10.1
S	-18 ± 20	20.4 ± 17.6	-4.9 ± 7.5

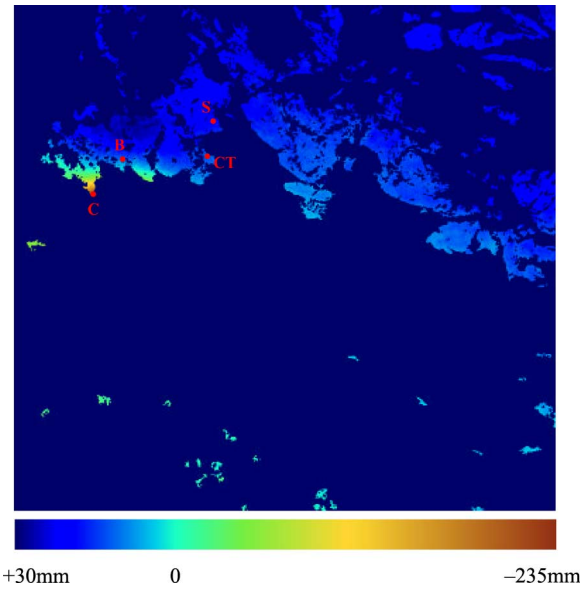

Fig. 13. Millimetric deformation map of the Gulf of Corinth obtained after atmospheric correction.

determine the global tropospheric model and are not disturbed by local effects.

To evaluate the performance of our approach, we compared the measured deformation before and after the tropospheric corrections to the deformation carried out by the GPS measurements available in the area (for the same period) [20]. Only four GPS points have been used for the comparison with our interferometric SAR (InSAR) analysis. This is caused by the incidence of two main aspects: 1) the time spanning of the GPS measurements of the Gulf of Corinth network [20] does not cover always the time spanning of our InSAR analysis and 2) the distribution of the coherence in the Gulf of Corinth area is not homogeneous.

The corrected results are much closer to the reference points than the raw data (see Table I). This comparison reveals that we reduce the tropospheric noise and improve the surface deformation accuracy. Points C and CT are in the area of earthquake displacement, whereas points B and S are in two different areas far from the earthquake (Table II). The maximum of deformation detected by GPS is located at point C.

Fig. 13 shows a deformation map corresponding to millimetric displacements for the studied area. The atmospheric correction has decreased the average uncertainty from ±26 to ±12 mm. Although the amount of data available for this paper was really important, we did not obtain a displacement model for the 1995 earthquake, which was really different with respect to the one obtained by previous work [21], [22].

D. Interests and Limits of the Proposed Method

One of the main advantages of the proposed method is that it does not rely on the knowledge of auxiliary data since it estimates the tropospheric contribution directly from interferograms at global and local scales. Besides, the number of interferograms is not a key point in the atmospheric correction, even if a high number of interferograms may improve the results.

The method limits rely on the phase/altitude correlation assumption, which supposes working on an area with strong topography. Applying this technique on flat areas will not allow the retrieval of global effects. Only local perturbations will be estimated and corrected.

Compared to the famous PS method [8], it should be noted that the stable-pixel selection criterion is intrinsically different. However, a preliminary study showed that some of the PS candidates are common to both methods [23]. It is specially the case in urban and rocky areas. However, in one case, pixel clusters are detected, whereas PS candidates are isolated points.

In order to make a rigorous comparison between the two methods, the whole PS inversion chain should be applied, and the results should be analyzed.

V. CONCLUSION

In this paper, we have presented a new methodological approach for detecting and removing atmospheric effects using a multitemporal database constituted by several differential interferograms. The performances of this technique have been verified for a region characterized by a strongly irregular topography as the Gulf of Corinth area. Therefore, this method is highly dependent of the coherence of the original interferograms and of the nature of the investigated area. Indeed, minimal variation of ground elevation is necessary to be able to estimate the phase/altitude correlation. This condition limits the use of this method for large urban areas usually built on flat terrain. However, in this case, the use of PSs has proven to be very efficient.

Further work includes the comparison between the proposed method and PS approaches.

REFERENCES

[1] D. M. Rossi, C. Carmona, F. Adragna, G. Peltzer, K. Feigl, and T. Rabaute, "The displacement field of the Landers earthquake mapped by radar interferometry," *Nature*, vol. 364, no. 6433, pp. 138–142, Jul. 1993.
[2] S. Usai, "A new approach for long term monitoring of deformations by differential SAR interferometry," Ph.D. dissertation, Delft Univ., Delft, The Netherlands, 2001.
[3] B. Fruneau, J. Achache, and C. Delacourt, "Observation and modeling of the Saint-Etienne-de-Tinée landslide using SAR interferometry," *Tectonophysics*, vol. 265, pp. 181–190, 1996.
[4] D. Massonnet, P. Briole, and A. Arnaud, "Deflation of Mount Etna monitored by spaceborne radar interferometry," *Nature*, vol. 375, no. 6532, pp. 567–570, 1995.
[5] D. Massonnet and K. L. Feigl, "Discrimination of geophysical phenomena in satellite radar interferograms," *Geophys. Res. Lett.*, vol. 22, no. 12, pp. 1537–1540, Jun. 1995.
[6] H. A. Zebker, P. A. Rosen, and S. Hensley, "Atmospheric effects in interferometric synthetic aperture radar surface deformation and topographic maps," *J. Geophys. Res.—Solid Earth*, vol. 102, no. B10, pp. 7547–7563, Apr. 1997.
[7] H. Tarayre and D. Massonnet, "Effects of refractive atmosphere on interferometric processing," in *Proc. IGARSS*, 1994, pp. 1717–1719.

[8] A. Ferretti, C. Prati, and F. Rocca, "Permanent scatterers in SAR interferometry," *IEEE Trans. Geosci. Remote Sens.*, vol. 39, no. 1, pp. 8–20, Jan. 2001.
[9] D. T. Sandwell and E. J. Price, "Phase gradient approach to stacking interferograms," *J. Geophys. Res.*, vol. 103, no. B12, pp. 30 183–30 204, 1998.
[10] F. Beauducel, P. Briole, and J.-L. Froger, "Volcano wide fringes in ERS SAR interferograms of Etna (1992–1998): Deformation or tropospheric effect?" *J. Geophys. Res*. vol. 105, pp. 16 391–16 402, 1999.
[11] F. Sarti, H. Vadon, and D. Massonnet, "A method for automatic characterization of InSAR atmospheric artefacts by correlation of multiple interferograms over the same site," in *Proc. IGARSS*, Hambourg, Germany, Jun. 1999, pp. 1937–1939.
[12] R. Touzi, A. Lopes, J. Bruniquel, and P. W. Vachon, "Coherence estimation for SAR imagery," *IEEE Trans. Geosci. Remote Sens.*, vol. 37, no. 1, pp. 135–149, Jan. 1999.
[13] E. Trouvé, J.-M. Nicolas, and H. Maître, "Fringe detection in noisy complex interferograms," *Appl. Opt.—Inf. Process.*, vol. 35, no. 20, pp. 3799–3806, Jul. 1996.
[14] F. Chaabane, A. Avallone, F. Tupin, P. Briole, and H. Maître, "Improvement of tropospheric correction by adapted phase filtering," in *Proc. EUSAR*, Cologne, Germany, Jun. 2002, pp. 361–364.
[15] F. Chaabane, "Suivi multitemporel en interférométrie radar et prise en compte des effets atmosphériques," Ph.D. dissertation, Univ. Paris XI, Orsay, France, Mar. 2004.
[16] I. Bloch, "Information combination operators for data fusion: A comparative review with classification," *IEEE Trans. Syst., Man, Cybern.*, vol. 26, no. 1, pp. 52–67, Jan. 1996.
[17] R. Bellman, "On a routing problem," *Q. Appl. Math.*, vol. 16, no. 1, pp. 87–90, 1958.
[18] D. C. Ghiglia and L. A. Romero, "Robust two-dimensional weighted and unweighted phase unwrapping that uses fast transforms and iterative methods," *J. Opt. Soc. Amer. A, Opt. Image Sci.*, vol. 11, no. 1, pp. 107–117, Jan. 1994.
[19] E. Trouvé, J.-M. Nicolas, and H. Maître, "Improving phase unwrapping techniques by the use of local frequency estimates," *IEEE Trans. Geosci. Remote Sens.*, vol. 36, no. 6, pp. 1963–1972, Nov. 1998.
[20] A. Avallone, P. Briole, A. M. Agatza-Balodimou, H. Billiris, O. Charade, C. Mitsakaki, A. Nercessian, K. Papazissi, D. Pradissis, and G. Veis, "Analysis of eleven years of deformation measured by GPS in the Corinth Rift laboratory area," *C. R. Geosci.*, vol. 336, no. 4/5, pp. 301–311, 2004.
[21] P. Bernard, P. Briole, B. Meyer, H. Lyon-Caen, J.-M. Gomez, C. Tiberi, C. Berge, R. Cattin, D. Hatzfeld, C. Lachet, B. Lebrun, A. Deschamps, F. Courbouleux, C. Larroque, A. Rigo, D. Massonnet, P. Papadimitriou, J. Kassars, D. Diagortas, K. Makropolus, G. Veis, E. Papazissi, C. Mitsakaki, V. Karkostas, E. Papadimitriou, D. Papanastassiou, G. Chouliars, and G. Stravakakis, "The $M_s = 6.2$ June 15, 1995 Aigion earthquake (Greece): Evidence for low angle normal faulting in the Corinth rift," *J. Seismol*., vol. 1, no. 2, pp. 131–150, 1997.
[22] A. Avallone and P. Briole, "Analyse de dix ans de déformation du rift de Corinthe (Grèce) par géodésie spatiale," Ph.D. dissertation, Inst. Phys. Globe de Paris, Paris, France, 2003.
[23] P. Lopez-Quiroz, J. M. Nicolas, F. Tupin, P. Briole, and F. Chaabane, "Permanent scatterers: Comparison of identification methods," in *Proc. EUSAR*, Dresden, Germany, May 2006.

Ferdaous Chaabane received the télécommunication engineering degree from the Higher School of Communication of Tunis (Sup'Com), Tunisia, in 1999, and the Ph.D. degree in image processing from the University of Paris XI, Orsay, France, in 2004. Her doctoral research includes multitemporal ground-deformation monitoring using differential SAR interferometry and multitemporal atmospheric effect correction.

She is currently with Sup'Com, where she is an Associate Professor at the Mathématiques Appliquées, Signaux et Communications Department and a Creator Member of the Research Unit in Satellite Images and Its Applications (URISA). Her research interests include SAR interferometry and image processing.

Antonio Avallone received the Master degree in geophysics from Naples University, Naples, Italy, in 1998, and the Ph.D. degree in geophysics from the Institut de Physique du Globe, Paris, France, working on the analysis of ten years of deformation in the Gulf of Corinth (Greece) by using both GPS and SAR interferometry techniques.

He is currently with the Istituto Nazionale di Geofisica e Vulcanologia, Grottaminarda, Italy, for the installation of a permanent GPS network in Italy and the relative data interpretation for active tectonics studies.

Florence Tupin received the engineering and Ph.D. degrees from the Ecole Nationale Supérieure des Télécommunications (ENST), Paris, France, in 1994 and 1997, respectively.

She is currently an Associate Professor in the Signal and Image Processing (TSI) Department, ENST. Her research interests include image analysis and interpretation, 3-D reconstruction, Markov random field techniques, and SAR remote sensing.

Pierre Briole received the Ph.D. degree in geophysics from the University of Paris VI, Paris, France, in 1990.

He is currently the Research Director at the French National Center for Research (CNRS), Paris. He is also with the Institut de Physique du Globe, Paris. His research interests include the measurement, modeling, and interpretation of ground deformation of volcanoes and seismic areas, using several geodetic and remote sensing techniques (e.g., GPS and SAR interferometry). His geographic research areas are mostly located around the Mediterranean basin.

Henri Maître received the engineering degree from the Ecole Centrale de Lyon, Lyon, France, in 1971, and the Docteur es Sciences degree in physics from the University of Paris VI, Paris, France, in 1982.

He has taught digital picture processing since 1973 at the Ecole Nationale Supérieure des Télécommunications (Telecom Paris), Paris, where he is a Professor. His research interests include image analysis, image understanding and computer vision, and applications in the domains of satellite and aerial image processing.